Model-Based Iterative Reconstruction of Magnetization Using Vector Field Electron Tomography

K. Aditya Mohan, *Member, IEEE*, Prabhat KC, Charudatta Phatak, Marc De Graef, and Charles A. Bouman, *Fellow, IEEE*

***Abstract*—Vector field electron tomography (VFET) is extensively used for three-dimensional (3-D) imaging of magnetic materials at nanometer resolutions. The conventional approach is to reconstruct and visualize the magnetic vector potential or the magnetic field associated with the sample. There is a lack of algorithms capable of reconstructing the 3-D distribution of magnetization from VFET data. Unlike magnetic vector potential and magnetic field, magnetization is a fundamental physical property of the sample that does not extend beyond the dimensions of the sample. We present a model-based iterative reconstruction algorithm (MBIR) that reconstructs the magnetization by minimizing a cost function consisting of a forward model term and a prior model term. The forward model uses the physics of imaging to model the VFET data as a function of the magnetization, and the prior model enforces sparsity in the magnetization reconstruction. We then formulate an optimization algorithm based on the theory of alternate direction method of multipliers to minimize the resulting MBIR cost function. Using simulated and real data, we show that our algorithm accurately reconstructs both the magnetization and the magnetic vector potential.**

***Index Terms*—Electron microscopy, image reconstruction, iterative algorithms, magnetic vector potential, magnetization, tomography, vector fields.**

I. Introduction

MAGNETIC particles with nanometer dimensions have unique quantum mechanical properties that are enabling new technologies in the fields of healthcare, life sciences, and material science [1]. In order to understand and quantify these magnetic nanostructures, there is a growing interest for new methods of imaging the magnetic vector fields. In particular, vector field electron tomography (VFET) was among the first methods for imaging magnetic field properties at nanometer scale [2].

In VFET, electrons from a transmission electron microscope (TEM) are focused on the sample and the intensity of the transmitted electrons after passing through the sample are measured by a planar detector. The sample is then tilted across an axis and measurements are made at multiple tilt angles as shown in Fig. 1. This procedure is then repeated across a tilt axis that is orthogonal to the earlier tilt axis. Next, the electron phase shift at each tilt angle is retrieved from detector measurements using the methods in [3], [4]. This procedure is known as phase retrieval and is achieved using either electron holography methods [5], [6] or through-focal series measurements in Lorentz TEM mode [3]. This is an essential step since information about the magnetic sample is contained in the phase shift rather than the intensity of the electrons exiting the sample.

The conventional approach to visualize a magnetic sample is to reconstruct a vector field called the magnetic vector potential or the magnetic field [2], [3], [5]. These vector fields exist both inside and outside the sample. To reconstruct these vector fields, the conventional approach is to rely on a direct analytical inversion of the standard Aharonov-Bohm [7] relation that expresses the electron phase shift as a linear function of the vector field projection [2]. This phase shift is the total electron phase shift and has contributions from the electrostatic and magnetic phase shifts. To isolate the magnetic contribution, the sign of the magnetic phase shift is flipped by flipping the sample across the direction of electron propagation. Then, the magnetic phase shift is computed as half the difference between the electron phase shifts before and after flipping the sample [2], [3], [5].

Manuscript received October 28, 2017; revised February 23, 2018 and April 7, 2018; accepted May 7, 2018. Date of publication May 18, 2018; date of current version August 13, 2018. This work was supported in part by computational resources provided by Information Technology at Purdue University, West Lafayette, IN, USA. The work of K. A. Mohan, M. De Graef, and C. A. Bouman was supported by an Air Force Office of Scientific Research/Multidisciplinary Research Program of the University Research Initiative Grant #FA9550-12-1-0458. The work of P. KC was supported in part by the National Science Foundation under Grant DMR-1564550. The work of C. Phatak was supported by the U.S. Department of Energy, Office of Science, Basic Energy Sciences, Materials Sciences and Engineering Division. Use of Center for Nanoscale Materials was supported by the U.S. Department of Energy, Office of Science, Office of Basic Energy Sciences, under Contract DE-AC02-06CH11357. LLNL-JRNL-731358, The Lawrence Livermore National Laboratory is operated by Lawrence Livermore National Security, LLC, for the U.S. Department of Energy, National Nuclear Security Administration under Contract DE-AC52-07NA27344. The associate editor coordinating the review of this manuscript and approving it for publication was Dr. Kees Joost Batenburg. *(Corresponding author: K. Aditya Mohan.)*

K. A. Mohan was with the School of Electrical and Computer Engineering, Purdue University, West Lafayette, IN 47907 USA. He is now with the Computational Engineering Division, Lawrence Livermore National Laboratory, Livermore, CA 94550 USA (e-mail: adityakadri@gmail.com).

P. KC and M. De Graef are with the Department of Material Science and Engineering, Carnegie Mellon University, Pittsburgh, PA 15213 USA (e-mail: prabhat.kc077@gmail.com; degraef@cmu.edu).

C. Phatak is with the Materials Science Division, Argonne National Laboratory, Lemont, IL 60439 USA (e-mail: cd@anl.gov).

C. A. Bouman is with the School of Electrical and Computer Engineering, Purdue University, West Lafayette, IN 47907 USA (e-mail: bouman@purdue.edu).

Digital Object Identifier 10.1109/TCI.2018.2838454

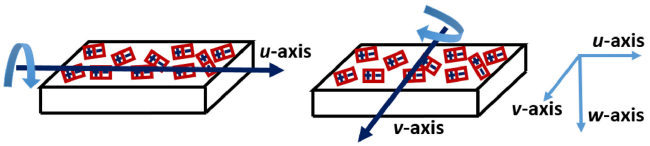

Fig. 1. Illustration of data acquisition in vector field electron tomography (VFET). In VFET, the sample is mounted on a rotary stage and exposed to electron radiation. The sample is then tilted across two orthogonal tilt axes (u-axis and v-axis) and measurements are made at multiple tilt angles.

Henceforth, anytime electron phase shift is mentioned in this paper, we are referring to the magnetic phase shift.

The algorithm presented in [2] is an analytic technique for reconstruction of the 3D magnetic vector potential using a variation of the filtered back-projection algorithm. It also assumes that the divergence of the magnetic vector potential is zero. The magnetic field is then computed as the curl of the magnetic vector potential. There also exist analytical methods to reconstruct the magnetic field directly from gradients of electron phase shift images [2], [5] while assuming zero divergence for the magnetic field in the (u, v, w) spatial coordinate axes. An algebraic reconstruction technique (ART) for unregularized reconstruction of magnetic fields is presented in [8]. All these methods result in reconstruction artifacts due to the ill-posed nature of the inverse problem [9]. The reconstruction can be fixed by acquiring a third set of tilt series where the rotation axis is perpendicular to the axes of the first two tilt series [9]. However, this technique is difficult to implement in practice.

There is a lack of regularized iterative reconstruction algorithms that enforce sparsity during reconstruction of the magnetic field and magnetic vector potential. Such algorithms have been widely used to reconstruct vector fields in other applications such as fluid flow and optical flow [10]–[15]. Regularized vector field reconstruction using penalty functions such as the L2-norm or L1-norm are presented in [11], [12]. There also exist techniques that allow us to use angular regularization for vector fields [16], [17]. More advanced methods that rely on regularizing the divergence and curl of the vector fields are presented in [18], [19].

Importantly, there is a need for algorithms that perform 3D reconstruction of a vector field called magnetization which is a fundamental material property of the sample. Magnetization expresses the position-dependent density of magnetic dipole moments within the magnetic sample. Note that all other vector fields such as magnetic vector potential and magnetic field are derived from the magnetization. It is challenging to perform 3D reconstruction of the magnetization from the phase shift data since the electron phase shift has a complex global dependence on the 3D distribution of magnetization. Thus, scientists typically settle for visualizing the magnetic vector potential or the magnetic field.

A model-based algorithm to reconstruct the in-plane component of magnetization in 2D is presented in [20]. It uses Tikhonov regularization to produce a unique 2D reconstruction of the magnetization using an iterative conjugate gradient algorithm. Similar iterative algorithms for 3D regularized reconstruction of magnetization from tomographic tilt series data are outlined in the abstracts [21]–[23]. These abstracts also stress the need for regularization and other constraints to solve the ill-posed problem of 3D magnetization reconstruction.

The framework of model-based iterative reconstruction (MBIR) has resulted in significant gains in a wide range of imaging applications such as X-ray computed tomography [24]–[31], bright field electron tomography [32], [33], and HAADF-STEM tomography [34]. In [35], we recently presented a model-based algorithm for 3D reconstruction of magnetic vector potential using VFET. MBIR is based on the estimation of a reconstruction that best fits a forward model and a prior model. The forward model uses the physics of imaging to express the measured data as a function of the unknown sample. The prior model regularizes the reconstruction of the sample using a suitable model of sparsity.

In this paper, we will use the framework of MBIR to formulate an algorithm that will reconstruct both magnetization and magnetic vector potential. This algorithm is presented in the conference abstract [36] and the Ph.D. thesis [37]. Our algorithm performs tomographic reconstruction of the 3D distribution of the magnetization vector field from the VFET data. Furthermore, it also significantly reduces the artifacts that are typically seen in reconstructions of magnetic vector potential using the conventional method [9].

Our approach to reconstruction uses the MBIR formulation to derive a cost function such that the reconstruction is the solution that minimizes the cost function. We show that gradient based optimization techniques result in inefficient implementations when directly applied to the resulting cost optimization problem. So, we will use variable splitting and the theory of alternate direction method of multipliers (ADMM) to solve the original minimization problem as an iterative solution to two simpler minimization problems. We show that the simpler minimization problems can be solved efficiently using existing optimization techniques such as iterative coordinate descent (ICD) [24] and gradient descent techniques [38]. We validate our algorithm by presenting reconstructions of both simulated and real experimental data. The software implementing this reconstruction algorithm is available for download at the link https://github.com/adityamnk/vfet_mbir.

The organization of this paper is as follows. In Section II, we present the forward and prior models for MBIR and formulate a cost function that when minimized yields a reconstruction of the magnetization. In Section III, we present an optimization algorithm to minimize the cost function derived in Section II. We present simulated and real data results in Section IV that validate the performance of our algorithm. Finally, we present our conclusions in Section V.

II. Model-Based Iterative Reconstruction (MBIR) of Magnetization

Our goal is to reconstruct the magnetization from the electron phase shift data. Let y be a vector of all the pixel values of the electron phase shift images at the various tilt angles and x be a vector of voxel values of all three vector components of magnetization. In the MBIR framework, the reconstruction, $\hat{x}$, is given by the solution to the optimization problem

$$\hat{x} = \underset{x}{\operatorname{argmin}} \left\{ -\log p(y|x) - \log p(x) \right\}, \tag{1}$$

where $\log p(y|x)$ is the forward model term that gives the log-likelihood of the data, y, given the object x and $\log p(x)$ is the prior model term that gives the log-likelihood of the object, x. We will next derive expressions for $\log p(y|x)$ and $\log p(x)$.

A. Forward Model

The forward model expresses the phase shift of the electrons, y, propagating through the sample as a function of the magnetization, x. The forward model has the form

$$y = FHx + w, \tag{2}$$

where F is the sparse tomographic projection matrix, H is a non-sparse convolution matrix that performs linear space-invariant convolution, and w is the noise vector.

This form of the forward model is derived by first expressing the magnetic vector potential as a function of the magnetization and then expressing the electron phase shift as a function of the magnetic vector potential. To do this, we first express the magnetic vector potential as a convolution of the magnetization with the vector form of the Green's function [39]. Let $r = (u, v, w)$ and $r' = (u', v', w')$ be position vectors in 3D space spanned by the mutually orthogonal (u, v, w) coordinates. Note that (u, v, w) are in the coordinate system of the sample and tilt along with the sample. Then, the magnetic vector potential, $A(r)$, is given by the convolution cross-product of the magnetization, $M(r)$, with a vector form of the Green's function, $h_C(r) = r/|r|^3$, as shown below [39], [40],

$$A(r) = \frac{\mu_0}{4\pi} \int_{\mathcal{R}^3} M(r') \times h_C(r - r') dr', \tag{3}$$

where $\times$ denotes the vector cross-product and μ_0 is the permeability of a vacuum. The magnetic field, $B(r)$, is then the curl of the magnetic vector potential given by $B(r) = \nabla \times A(r)$. In (3), the integration is performed over a spatial domain that completely contains the sample. This ensures that there is no error due to the finite domain of integration since magnetization is zero outside the boundaries of the sample. During reconstruction, the user specifies the total size of the volume that must be reconstructed. For instance, if the sample is contained within the field of view (FOV) of the detector, then the user can specify the reconstructed volume to simply be the region within the detector FOV.

In order to numerically compute the convolution in (3), we must represent it with a discrete approximation as derived in Appendix V. To do this, we will represent the three components of the vector field $A(r)$ by the three discrete vectors $z^{(u)}$, $z^{(v)}$, and $z^{(w)}$. So for example, $z^{(u)}$ is a discretization of the u-axial component of the continuous 3D magnetic vector potential. Similarly, $x^{(u)}$, $x^{(v)}$, and $x^{(w)}$ represent the three discretized components of the magnetization vector field $M(r)$. Using this notation, equation (3) can be expressed in discrete form as

$$z^{(u)} = H^{(w)} x^{(v)} - H^{(v)} x^{(w)}, \tag{4}$$

$$z^{(v)} = H^{(u)} x^{(w)} - H^{(w)} x^{(u)}, \tag{5}$$

$$z^{(w)} = H^{(v)} x^{(u)} - H^{(u)} x^{(v)}, \tag{6}$$

where $H^{(u)}$, $H^{(v)}$, and $H^{(w)}$ are matrices that implement 3D convolution with point spread functions given by

$$h_D^{(u)}[i, j, k] = w[i, j, k] \frac{i\Delta}{|i^2 + j^2 + k^2|^{3/2}}, \tag{7}$$

$$h_D^{(v)}[i, j, k] = w[i, j, k] \frac{j\Delta}{|i^2 + j^2 + k^2|^{3/2}}, \tag{8}$$

$$h_D^{(w)}[i, j, k] = w[i, j, k] \frac{k\Delta}{|i^2 + j^2 + k^2|^{3/2}}, \tag{9}$$

where $[i, j, k]$ are discrete coordinates, Δ is the voxel width, $h_D^{(u)}[0, 0, 0] = h_D^{(v)}[0, 0, 0] = h_D^{(w)}[0, 0, 0] = 0$, and $w[i, j, k]$ is a 3D Hamming window. Appendix A provides additional details about the Hamming window and zero-padding that is used to prevent aliasing during convolution.

Thus, we have that

$$z = Hx, \tag{10}$$

where $z = \left[z^{(u)t}, z^{(v)t}, z^{(w)t}\right]^t$, $x = \left[x^{(u)t}, x^{(v)t}, x^{(w)t}\right]^t$, and

$$H = \begin{bmatrix} 0 & H^{(w)} & -H^{(v)} \\ -H^{(w)} & 0 & H^{(u)} \\ H^{(v)} & -H^{(u)} & 0 \end{bmatrix}. \tag{11}$$

Next, we express the electron phase shift at each view as the projection of the magnetic vector potential component along the direction of electron propagation [39]. During a VFET experiment, the sample is first tilted across the u-axis and measurements are made at several tilt angles. The procedure is then repeated by tilting the sample across the v-axis and making additional measurements at multiple tilt angles. At each tilt angle, the phase shift of the electrons exiting the sample is recovered from measurements.

The phase shift of the electrons propagating along the positive w-axis is given by [2], [41],

$$\phi(r_\perp) = \frac{2\pi e}{h} \int A(r_\perp + l\hat{w}) \cdot \hat{w} dl \tag{12}$$

where $r_\perp$ is a 2D position vector on the projection plane, $\hat{w}$ is a unit vector directed along the positive w-axis, h is the Planck's constant, and e is the electron charge.

Let $y_i^{(u)}$ be a vector array containing all the pixel values of the electron phase image at the ith tilt angle for tilt across the u-axis. When the sample is tilted across the u-axis, the components of the magnetic vector potential along the v-axis and w-axis change direction as shown in Fig. 2. However, the direction of the vector component $z^{(u)}$ will always be perpendicular to the propagation direction (positive w-axis) since the direction of $z^{(u)}$ does not change when tilting across u-axis. Thus, the dot product in (12) ensures that only the $z^{(v)}$ and $z^{(w)}$ components of the magnetic vector potential will have a influence on the phase shift. If $P_i^{(u)}$ denotes the projection matrix that implements the line integral in (12) at a clockwise tilt angle of $\theta_i^{(u)}$ across the u-axis, we can show that,

$$y_i^{(u)} = -P_i^{(u)} z^{(v)} \sin\left(\theta_i^{(u)}\right) + P_i^{(u)} z^{(w)} \cos\left(\theta_i^{(u)}\right). \tag{13}$$

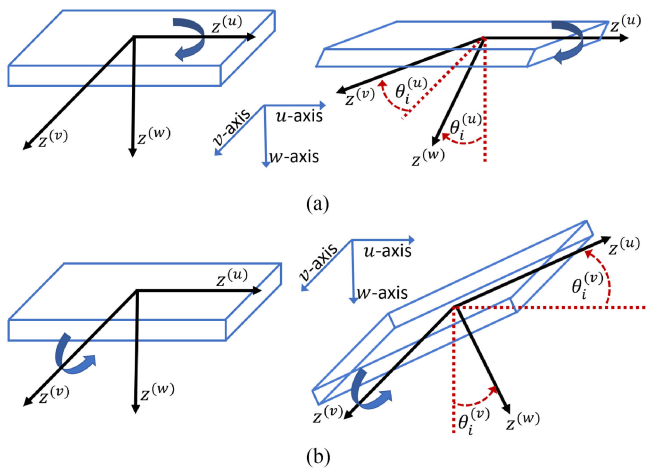

Fig. 2. Illustration of sample tilt across u-axis and v-axis. (a) shows how the $z^{(v)}$ and $z^{(w)}$ components of magnetic vector potential change direction when tilting across u-axis. (b) shows how the $z^{(u)}$ and $z^{(w)}$ components of magnetic vector potential change direction when tilting across v-axis. Note that $z^{(u)}$, $z^{(v)}$, and $z^{(w)}$ are attached to the coordinate frame of the sample.

Similarly, only the $z^{(u)}$ and $z^{(w)}$ components will influence the phase shift for tilt across the v-axis. In this case, the vector component $z^{(v)}$ will always be perpendicular to the propagation direction since the direction of $z^{(v)}$ does not change when tilting across v-axis. If $P_j^{(v)}$ denotes the projection matrix that implements the line integral in (12) at a anticlockwise tilt angle of $\theta_i^{(v)}$ across the v-axis, we can show that,

$$y_j^{(v)} = -P_j^{(v)} z^{(u)} \sin\left(\theta_j^{(v)}\right) + P_j^{(v)} z^{(w)} \cos\left(\theta_j^{(v)}\right). \quad (14)$$

Note that our framework allows for a different number of tilt angles across the u-axis and v-axis.

Then, we can express the relations in (13) and (14) in the form of matrix-vector products as,

$$y_i^{(u)} = F_i^{(u)} \begin{bmatrix} z^{(u)} \\ z^{(v)} \\ z^{(w)} \end{bmatrix} \text{ and } y_j^{(v)} = F_j^{(v)} \begin{bmatrix} z^{(u)} \\ z^{(v)} \\ z^{(w)} \end{bmatrix} \quad (15)$$

where

$$F_i^{(u)} = \left[0, \quad -P_i^{(u)} \sin\left(\theta_i^{(u)}\right), \quad P_i^{(u)} \cos\left(\theta_i^{(u)}\right)\right] \quad (16)$$

$$F_j^{(v)} = \left[-P_j^{(v)} \sin\left(\theta_j^{(v)}\right), \quad 0, \quad P_j^{(v)} \cos\left(\theta_j^{(v)}\right)\right]. \quad (17)$$

Let y be a vector array that concatenates all the vectors $y_i^{(u)}$ and $y_j^{(v)}$ for all the tilt angles indexed by i and j. We can then express y in terms of z as

$$y = Fz + w, \quad (18)$$

where w is the noise vector and F is a matrix that implements the linear relation in (15) for all indices i and j by appropriately stacking the matrices $F_i^{(u)}$ and $F_j^{(v)}$.

By substituting (10) in (18), we get the forward model

$$y = FHx + w, \quad (19)$$

where F represents the tomographic projection matrix and H represents the Green's function convolution matrix.

The forward log-likelihood function under the Gaussian noise assumption in (19) is then given by

$$-\log p(y|x) = \frac{1}{2\sigma^2} ||y - FHx||^2 + \text{ constant}, \quad (20)$$

where σ^2 is the variance of noise.

B. Prior Model

For the prior model, we use a Gaussian Markov Random Field (GMRF) [42] potential function to regularize the magnitude squared of the gradient of the magnetization. The expression for the prior log-likelihood function is

$$-\log p(x) = \sum_{\{k,l\}\in\mathcal{N}} \frac{w_{kl}}{2\sigma_x^2} \left[\left(x_k^{(u)} - x_l^{(u)}\right)^2 + \left(x_k^{(v)} - x_l^{(v)}\right)^2 + \left(x_k^{(w)} - x_l^{(w)}\right)^2\right] + \text{ constant}, \quad (21)$$

where σ_x is the regularization parameter and $\mathcal{N}$ is the set of all pairwise cliques in 3D space (set of all pairwise indices of neighboring voxels). The weight parameter w_{kl} is set such that it is inversely proportional to the spatial distance between voxels indexed by k and l. Also, $\sum_{l\in\mathcal{N}_k} w_{kl} = 1$, where $\mathcal{N}_k$ is the set of all indices of neighbors of voxel x_k. We can then express the prior model as

$$-\log p(x) = \frac{1}{2}\left[x^{(u)t}\tilde{B}x^{(u)} + x^{(v)t}\tilde{B}x^{(v)} + x^{(w)t}\tilde{B}x^{(w)}\right] + \text{ constant}, \quad (22)$$

where $\tilde{B}$ is a matrix such that

$$\tilde{B}_{k,l} = \begin{cases} 1/\sigma_x^2 & \text{if} \quad k = l \\ -w_{kl}/\sigma_x^2 & \text{if} \quad l \in \mathcal{N}_k \end{cases}. \quad (23)$$

The prior model in terms of $x = \left[x^{(u)t}, x^{(v)t}, x^{(w)t}\right]^t$ is given by

$$-\log p(x) = \frac{1}{2}x^t Bx + \text{constant}, \quad (24)$$

where

$$B = \begin{bmatrix} \tilde{B} & 0 & 0 \\ 0 & \tilde{B} & 0 \\ 0 & 0 & \tilde{B} \end{bmatrix}. \quad (25)$$

C. Cost Function

The reconstruction is then obtained by solving the optimization problem

$$\hat{x} = \underset{x}{\text{argmin}} \left\{\frac{1}{2\sigma^2} ||y - FHx||^2 + \frac{1}{2}x^t Bx\right\}. \quad (26)$$

Even though (26) can be solved directly using gradient descent algorithms [38], such implementations are inefficient since FH and its transpose $(FH)^t$ cannot be implemented using fast

Fourier transforms due to the presence of the projection matrix F. Due to the presence of the convolution matrix H in (26), it is also not possible to solve this problem by adapting fast reconstruction algorithms such as [24], [43] developed in the field of X-ray computed tomography.

Our approach solves the magnetization reconstruction problem by iteratively solving two simpler optimization problems that allow for highly efficient algorithmic solutions [37]. We will use variable splitting and the theory of alternate direction method of multipliers [44] to perform reconstruction by alternately solving a tomographic reconstruction problem and a deconvolution problem. The tomographic reconstruction problem is described in Section III-A and is solved by adapting an implementation of the fast tomographic reconstruction algorithm in [24]. The deconvolution problem is presented in Section III-B and is solved using a gradient descent algorithm that uses fast Fourier transform (FFT) for rapid calculation of gradient and optimal step size.

To formulate our reconstruction algorithm, we will express the unconstrained problem in equation (26) as a constrained optimization problem of the form

$$(\hat{x},\hat{z}) = \underset{x,z}{\operatorname{argmin}} \left\{ \frac{1}{2\sigma^2} ||y - Fz||^2 + \frac{1}{2} x^t B x \right\} \text{s.t. } z = Hx. \tag{27}$$

The augmented Lagrangian function [44] for this constrained optimization problem is

$$L(x,z;t) = \frac{1}{2\sigma^2} ||y - Fz||^2 + \frac{\mu}{2} ||Hx - z + t||^2 + \frac{1}{2} x^t B x, \tag{28}$$

where z is the auxiliary vector, t is the scaled dual vector, and $\mu > 0$ is the augmented Lagrangian parameter.

III. Optimization Algorithm

To solve the augmented Lagrangian formulation of the optimization problem, we use the theory of alternate direction method of multipliers (ADMM). Using the ADMM method [44], we can show that the optimization algorithm that solves (27) is given by Algorithm 1. Thus, the original minimization problem in (26) is solved by iteratively solving simpler minimization problems shown in (29) and (30). Our modular framework allows us to develop independent software modules to solve (29) and (30). Both (29) and (30) can be solved efficiently using a variety of well known optimization algorithms. We solve (29) using the steepest gradient descent algorithm [38] and (30) using a variant of the iterative coordinate descent algorithm [24].

In Algorithm 1, we use an adaptive update strategy [44]–[46] for the augmented Lagrangian parameter μ. We update μ based on the primal and dual residuals at each ADMM iteration. The primal residual is defined as $r = \hat{z} - H\hat{x}$ and the dual residual is defined as $s = \hat{z} - z^{(\text{old})}$, where $\hat{x}$ and $\hat{z}$ are the estimates after performing the updates in (29) and (30) and $z^{(old)}$ is the estimate before performing the update. If the primal residual is greater than γ times the dual residual, we increase the parameter μ by a factor of τ, where $\gamma > 1$ and $\tau > 1$. Similarly, if the dual residual is greater than γ times the primal residual, we decrease the parameter μ by a factor of τ. The idea here is to keep the norms of the primal and dual residuals within a factor of γ from one another. As the iterations progress, both the primal and dual residuals converge to zero. Note that the scaled dual vector t must also be updated appropriately after updating μ [44].

Algorithm 1: Reconstruction.

1: Initialize $\hat{x}, \mu, \tau, \gamma$
2: $\hat{z} \leftarrow H\hat{x}, t \leftarrow zero\ vector$
3: **while** not converged **do**
4: $z^{(old)} \leftarrow \hat{z}$
5: DECONVOLUTION -

$$\hat{x} \leftarrow \underset{x}{\operatorname{argmin}} \left\{ \frac{\mu}{2} ||Hx - \hat{z} + t||^2 + \frac{1}{2} x^t B x \right\} \tag{29}$$

6: TOMOGRAPHIC INVERSION -

$$\hat{z} \leftarrow \underset{z}{\operatorname{argmin}} \left\{ \frac{1}{2\sigma^2} ||y - Fz||^2 + \frac{\mu}{2} ||H\hat{x} - z + t||^2 \right\} \tag{30}$$

7: $t \leftarrow t + (H\hat{x} - \hat{z})$
8: $r \leftarrow (\hat{z} - H\hat{x})$ // compute primal residual
9: $s \leftarrow \left(\hat{z} - z^{(old)}\right)$ // compute dual residual
10: **if** $||s||_2 > \gamma ||r||_2$ **then**
11: $\mu \leftarrow \mu/\tau$
12: $t \leftarrow \tau t$
13: **end if**
14: **if** $||r||_2 > \gamma ||s||_2$ **then**
15: $\mu \leftarrow \tau \mu$
16: $t \leftarrow t/\tau$
17: **end if**
18: **end while**

A. Tomographic Inversion

The solution to the minimization problem in (30) is the value of z that minimizes the cost function

$$g(z) = \frac{1}{2\sigma^2} ||y - Fz||^2 + \frac{\mu}{2} ||H\hat{x} - z + t||^2 . \tag{31}$$

To minimize (31), we will use a variant of the iterative coordinate descent (ICD) algorithm [24]. In this algorithm, we sequentially minimize (31) with respect to the magnetic vector potential value $z_k = \left[z_k^{(u)}, z_k^{(v)}, z_k^{(w)}\right]^t$ at each voxel location k while keeping the voxel values at other locations fixed. We repeat this minimization procedure for each voxel chosen in a random order until the algorithm converges.

To minimize (31) with respect to z_k while keeping other voxel values constant, we will reformulate (31) in terms of just z_k while ignoring all terms that do not depend on z_k. Let $\hat{z}_k$ denote the current estimate for z_k before performing the update. The cost function with respect to z_k is

$$g_{vox}(z_k) = \omega^t z_k + \frac{1}{2} (z_k - \hat{z}_k)^t \Omega (z_k - \hat{z}_k) + \frac{\mu}{2} ||\tilde{z}_k - z_k + t_k||^2 , \tag{32}$$

Algorithm 2: Tomographic Inversion.

Initialize $e_i^{(u)}$ and $e_j^{(v)}$ using (33) and (34).
while not converged **do**
  for all voxel indices k **do**
    $z'_k \leftarrow \hat{z}_k$
    Compute ω using (62), (63), and (64).
    Compute Ω using (65), (66), (67), (68), (69), and (70).
    Compute $\tilde{z}_k$ by substituting $\hat{x}$ in (35).
    $z'_k \leftarrow (\Omega + \mu I)^{-1} (-\omega + \Omega z'_k + \mu \tilde{z}_k + \mu t_k)$
    $e_i^{(u)} \leftarrow e_i^{(u)} + F_{i,*,k}^{(u)} (\hat{z}_k - z'_k)$
    $e_j^{(v)} \leftarrow e_j^{(v)} + F_{j,*,k}^{(v)} (\hat{z}_k - z'_k)$
    $\hat{z}_k \leftarrow z'_k$
  end for
end while

where ω and Ω are the respective gradient and Hessian of $\frac{1}{2\sigma^2} ||y - Fz||^2$ with respect to z_k and $\tilde{z}_k$ is a parameter that depends on $\hat{x}$. Expressions for ω and Ω are derived in Appendix B where we show that ω and Ω depend on $\hat{z}$ through the error sinogram parameters

$$e_i^{(u)} = y_i^{(u)} - F_i^{(u)} \hat{z} \text{ and} \tag{33}$$

$$e_j^{(v)} = y_j^{(v)} - F_j^{(v)} \hat{z}. \tag{34}$$

We will see that the error sinogram vectors allow for efficient implementation of the ICD algorithm. The value of $\tilde{z}_k$ is

$$\tilde{z}_k = \begin{bmatrix} H_{k,*}^{(w)} \hat{x}^{(v)} - H_{k,*}^{(v)} \hat{x}^{(w)} \\ H_{k,*}^{(u)} \hat{x}^{(w)} - H_{k,*}^{(w)} \hat{x}^{(u)} \\ H_{k,*}^{(v)} \hat{x}^{(u)} - H_{k,*}^{(u)} \hat{x}^{(v)} \end{bmatrix}, \tag{35}$$

where $H_{k,*}^{(u)}$, $H_{k,*}^{(v)}$, and $H_{k,*}^{(w)}$ denote the elements along the kth row of the matrices $H^{(u)}$, $H^{(v)}$, and $H^{(w)}$ respectively. Note that minimization of the cost function (32) with respect to z_k is equivalent to minimizing (31) while assuming constant values for other voxels. Since (32) is quadratic in z_k, there exists a closed-form expression for the value of z_k that minimizes (32). Thus, the new update for z_k is

$$\hat{z}_k \leftarrow (\Omega + \mu I)^{-1} (-\omega + \Omega \hat{z}_k + \mu \tilde{z}_k + \mu t_k). \tag{36}$$

where ω and Ω are given in Appendix B.

The optimization algorithm that minimizes the cost function in (31) is shown in Algorithm 2. The error sinograms, $e^{(u)}$ and $e^{(v)}$, are precomputed at the beginning of the algorithm. After each voxel update, only a few values in the error sinograms are updated depending on the non-zero elements of $F_{i,*,k}^{(u)}$ and $F_{j,*,k}^{(v)}$.

Algorithm 3: Deconvolution.

Compute Q from (39).
while not converged **do**
  $x' \leftarrow \hat{x}$
  Compute $g \leftarrow \mu H^t (Hx' - \hat{z} + t) + Bx'$.
  Compute $\alpha \leftarrow \frac{g^t g}{g^t Q g}$
  $\hat{x} \leftarrow x' - \alpha g$
end while

B. Deconvolution

The solution to the minimization problem in (29) is given by the value of x that minimizes the cost function

$$f(x) = \frac{\mu}{2} ||Hx - \hat{z} + t||^2 + \frac{1}{2} x^t B x. \tag{37}$$

We will use the steepest gradient descent algorithm [38] to iteratively minimize (37) with respect to the magnetization, x, until the algorithm converges. Gradient descent is based on the idea that the cost function (37) reduces in the direction of its negative gradient. By choosing an optimal step size that minimizes the cost in that direction, we will get closer to the global minimum of (37). Since the cost function in (37) is convex, our algorithm converges to the global minimum [38].

To formulate the optimization algorithm, we will derive expressions for the gradient, g, and Hessian, Q, of the cost function $f(x)$. In every iteration, we will update x in the direction of the negative gradient, $-g$. Since $f(x)$ is quadratic in x, there exists a closed form expression for the stepsize, α, that minimizes $f(x)$ in the direction of $-g$. The gradient of $f(x)$ is

$$g = \nabla f(x) = \mu H^t (Hx - \hat{z} + t) + Bx \tag{38}$$

and the Hessian of $f(x)$ is

$$Q = \mu H^t H + B. \tag{39}$$

Since (37) is quadratic, the optimal stepsize α can be shown to be [38]

$$\alpha = \frac{g^t g}{g^t Q g}. \tag{40}$$

Thus, the optimization algorithm that minimizes (37) is shown in Algorithm 3.

Note that directly computing the expressions in (38) and (40) using matrix-vector multiplication is computationally intensive. Instead, by formulating these expressions in terms of $H^{(u)}$, $H^{(v)}$, and $H^{(w)}$ that represent linear space invariant filtering matrices as shown in appendix C, we can efficiently compute (38) and (40) [42].

C. Algorithm Initialization

Since the cost function in (26) is convex, our optimization algorithm (Algorithm 1) is convergent. We use multi-resolution initialization [24], [47] to improve convergence speed. In this method, we reconstruct the magnetic vector potential and magnetization vector fields at coarse resolution scales and use the solution to initialize the reconstruction at finer scales. We use

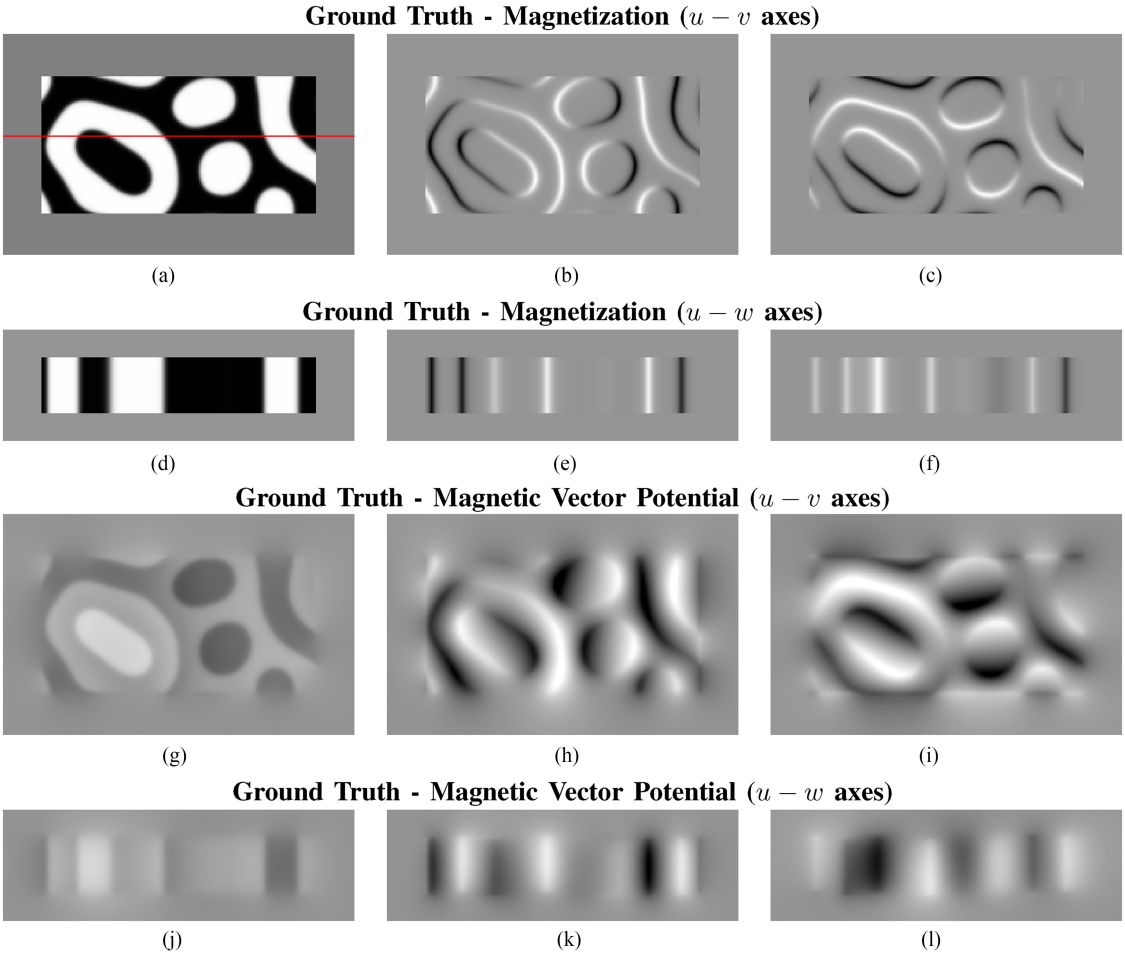

Fig. 3. Ground-truth of magnetization and magnetic vector potential. (a)–(c) and (d)–(f) show slices of the magnetization vector field along the $u-v$ plane (perpendicular to electron propagation) and $u-w$ plane (parallel to electron propagation) respectively. Similarly, (g)–(i) and (j)–(l) show slices of the magnetic vector potential along the $u-v$ plane and $u-w$ plane respectively. The 1st, 2nd, and 3rd columns show the vector field components oriented along the w-axis, v-axis, and u-axis respectively. Note that (d)–(f) and (j)–(l) show slices in the $u-w$ plane that lie along the red line in (a).

$N=3$ number of multi-resolution stages during reconstruction such that the voxel width at the nth multi-resolution stage is $2^{N-n}\Delta$, where $1 \leq n \leq N$ and Δ is the voxel width at the finest resolution scale. Hence, $n=1$ corresponds to reconstruction at the lowest voxel resolution and $n=N$ corresponds to reconstruction at the highest voxel resolution. In Algorithm 1, we set $\gamma = 10$ and $\tau = 2(N-n+1)$ at the nth multi-resolution stage of reconstruction. At the coarsest resolution scale, we start by initializing the magnetization and magnetic vector potential reconstructions to zeros. The voxel width of the reconstruction at the finest resolution scale is equal to the pixel width of the input phase shift images. The prior model regularization parameter σ_x is set empirically such that we get the best visual quality of reconstruction. The noise variance σ^2 is estimated from a uniform region in the data. The ratio $\beta = \frac{\sigma^2}{\sigma_x^2}$ is a measure of the relative influence of the forward and prior models on the reconstruction. Increasing β tends to favor the prior model resulting in reduced noise and increased smoothness in the reconstruction. Alternatively, reducing β favors the forward model resulting in sharper and more noisy reconstruction.

IV. Experimental Results

A. Simulated Data Results

In this section, we present reconstructions of simulated data using the new MBIR algorithm and compare it to reconstructions using traditional methods.

1) Data: We will generate simulated data from a phantom that is representative of the magnetization states observed in magnetic materials. The magnetization of a sample is described using the concept of magnetic domains i.e., regions in the sample where the neighboring magnetization vectors are oriented in the same direction. The 3D magnetization ground truth of a Ni_2MnGa simulated phantom is shown in Fig. 3(a)–(f). The bright regions in Fig. 3(a) and (d) correspond to magnetic domains where the magnetization direction is oriented along the positive w-axis. Similarly, the dark regions in Fig. 3(a) and (d) correspond to magnetic domains oriented along the negative w-axis. Near the interface between the bright and dark regions, we can see the domain walls where the magnetization changes direction. This change in direction can be visualized by observing

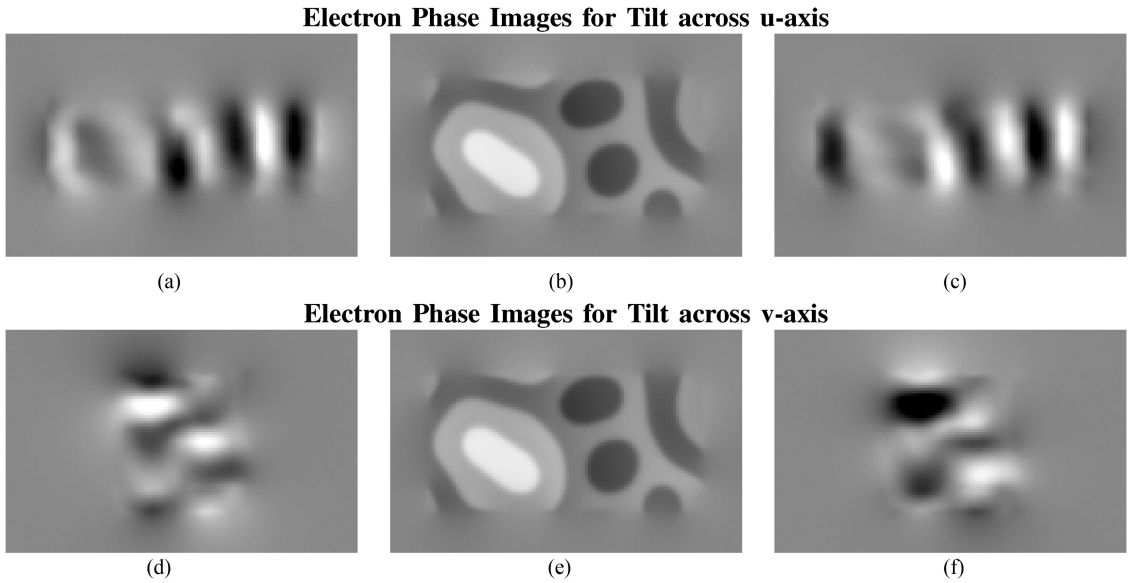

Fig. 4. Simulated phase shift data generated from magnetization ground-truth phantom. (a)–(c) and (d)–(f) show the simulated electron phase shift images for various tilt angles when the sample is tilted across the u-axis and v-axis respectively. The 1st, 2nd, and 3rd columns correspond to the tilt angles -70°, 0°, and 70° respectively.

the v, u-axial components of magnetization shown in Fig. 3(b), (e) and (c), (f).

The magnetization results in a magnetic vector potential that is simulated using (10). The magnetic vector potential ground truth is shown in Fig. 3(g)–(l). As the electrons in a TEM experiment propagate through the magnetic sample they undergo a change in phase. We forward project the magnetic vector potential using the expression in (18) to generate the electron phase shift images at multiple tilt angles for both the u-axis tilt series and v-axis tilt series. We simulate electron phase images at tilt angles ranging from -70° to 70° at steps of 2° for tilt across both the u-axis and v-axis. The simulated electron phase images at tilt angles of -70°, 0°, and 70° across the u-axis are shown in Fig. 4(a)–(c). Similarly, the electron phase images at the same angles but for tilt across the v-axis are shown in Fig. 4(d)–(f). Note that even though the number of tilt angles across the two axes are the same in this simulation, it is not a pre-requisite for our reconstruction algorithm. Also, the simulated angular range of -70° to 70° is reminiscent of typical TEM microscopy setups that do not permit data acquisition over a complete 180° angular range.

2) Reconstruction: Fig. 5(a)–(f) shows the MBIR reconstruction of the 3D magnetization from the simulated phase shift data. Since we could not find any other implementation of an algorithm to reconstruct the 3D magnetization in the literature, there is no other conventional reconstruction shown. Notice that the reconstruction accurately corresponds to the ground truth images shown in Fig. 3(a)–(f). The normalized root mean square error (NRMSE)[1] for the w, v, and u components of magnetization relative to the ground truth are 7.66%, 4.29% and 4.33% respectively.

Fig. 5(g)–(r) shows the reconstruction of the 3D magnetic vector potential from the simulated data using both MBIR and the conventional method presented in [2]. The conventional method in [2] is an algorithm that reconstructs magnetic vector potential using a filtered back projection algorithm. It uses an additional constraint that the divergence of magnetic vector potential is zero to reduce the feasible solution space. The drawback of this algorithm is the artifacts seen in Fig. 5(k) and (l). These artifacts are caused since [2] uses an analytical solution that results in singularities when solving the inverse problem.

In Table I, we compare the NRMSE[2] for the two reconstruction methods and Fig. 6 shows line plots through the sample for the reconstructions and ground truth. Table I shows that the NRMSE is much lower for MBIR than for the conventional method. This can also be seen in the line plots of Fig. 6 in which the MBIR line is close to the ground truth while the conventional reconstruction is much less accurate. In addition, notice that the v and u components of the conventional reconstruction shown in Fig. 5(k) and (l) have substantial vertical streaking artifacts that are not in the MBIR reconstructions.

The MBIR algorithm has a longer run-time when compared to the conventional method since MBIR is an iterative algorithm that reconstructs both magnetization and magnetic vector potential. In contrast, the conventional method is an analytical filtered back-projection algorithm that only reconstructs magnetic vector potential. The MBIR algorithm reconstructed the simulated data in 27.5 minutes while the conventional method completed the reconstruction in 3.5 minutes.

3) Experimental Parameters: Both the magnetization and magnetic vector potential ground truths have a size of $256 \times 256 \times 256$ and a voxel width of 2.5 nm. Each simulated phase image has a size of 128×128 and a pixel size of 5 nm. We also add Gaussian noise to the simulated phase images such that the average SNR is 56.85 dB. Note that the magnetization has

[1]Normalized using the simulated magnitude of magnetization of the sample.

[2]Normalized using the maximum magnitude of magnetic vector potential ground-truth.

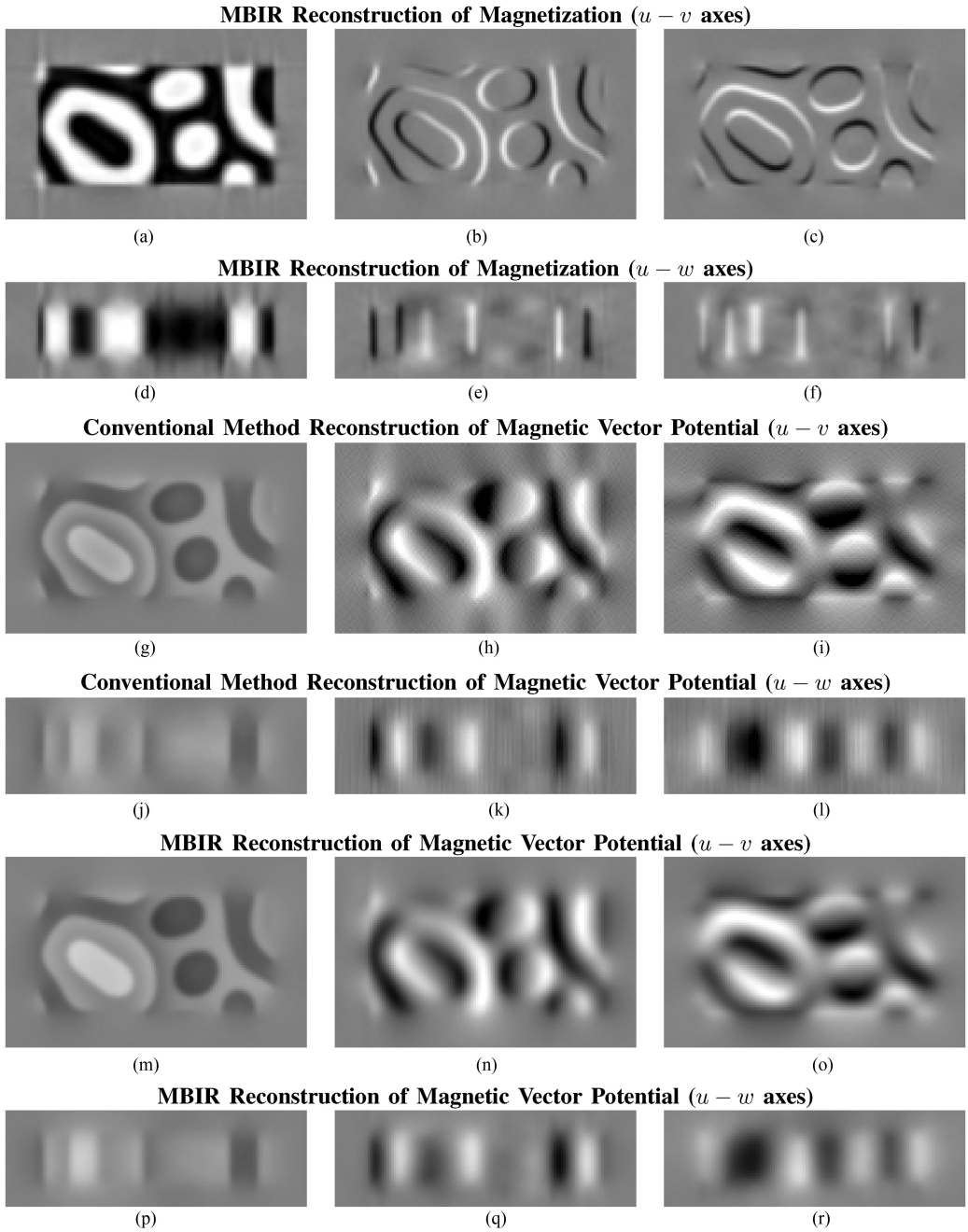

Fig. 5. Comparison of reconstructions of magnetization and magnetic vector potential using the conventional method and MBIR. (a)–(c) and (d)–(f) show the reconstruction of magnetization using MBIR along the $u-v$ plane and $u-w$ plane respectively. (g)–(i) and (j)–(l) show the reconstruction of magnetic vector potential using the conventional method along the $u-v$ plane and $u-w$ plane respectively. (m)–(o) and (p)–(r) show the reconstruction of magnetic vector potential using MBIR along the $u-v$ plane and $u-w$ plane respectively. The 1st, 2nd, and 3rd columns show the vector field components oriented along the w-axis, v-axis, and u-axis respectively. The conventional method reconstruction of magnetic vector potential results in artifacts as seen in (k) and (l). We can see that MBIR accurately reconstructs both the magnetic vector potential and magnetization of the sample.

TABLE I
NRMSE (NM^{-1}) BETWEEN THE MAGNETIC VECTOR POTENTIAL RECONSTRUCTION AND THE GROUND-TRUTH FOR SIMULATED DATA

	Conventional Method	MBIR
w-axial component	5.6%	0.46%
v-axial component	10.07%	0.88%
u-axial component	10.03%	0.85%

a constant magnitude of 4×10^{-5} nm^{-2} within the sample (the inner rectangular region in Fig. 3(a)–(f)). All reconstructions have a size of $128 \times 128 \times 128$ in 3D space and a voxel size of 5 nm.

The phase shift images in Fig. 4(a)–(f) are scaled from a minimum of -1.2 radians to a maximum of 1.1 radians. The images showing the magnetic vector potential in Figs. 3(g)–(l) and 5(g)–(r) are scaled from a minimum of -11×10^{-3} nm^{-1} to a maximum of 11×10^{-3} nm^{-1}. The images of magnetization in Figs. 3(a)–(f) and 5(a)–(f) are scaled from a minimum of -4×10^{-5} nm^{-2} to a maximum of 4×10^{-5} nm^{-2}.

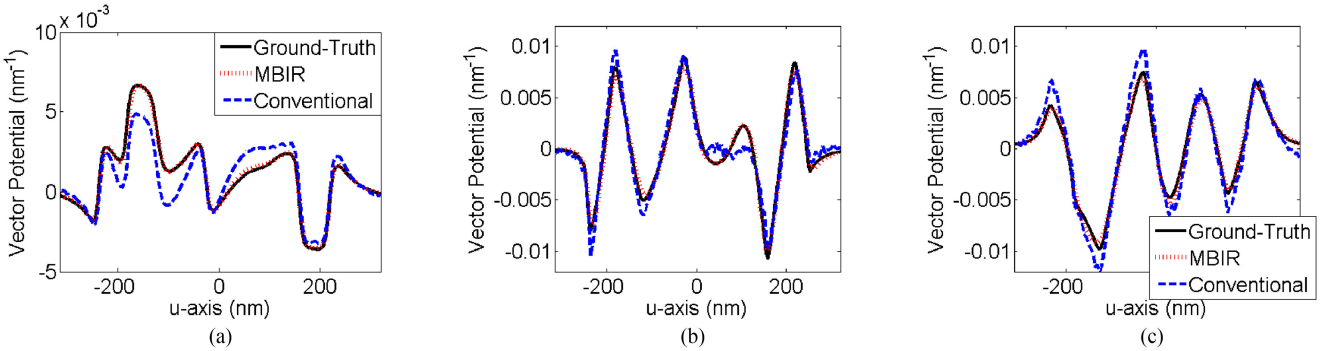

Fig. 6. Line plot comparison of magnetic vector potential. The above curves are along the red colored line in Fig. 3(a). We can see that all components of the magnetic vector potential reconstruction using MBIR accurately follows the ground-truth.

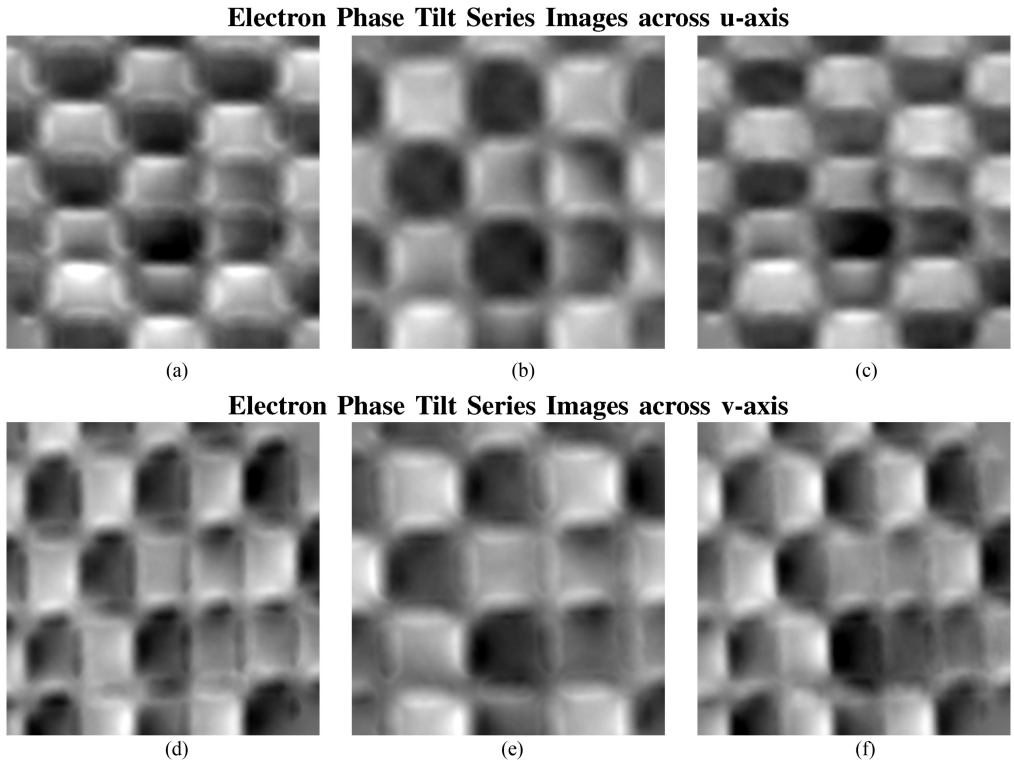

Fig. 7. Electron phase images of a Ni-Fe sample acquired using a TEM. (a)–(c) and (d)–(f) show the phase images at various tilt angles for tilt across the u-axis and v-axis respectively. (a,d), (b,e), and (c,f) are phase images at tilt angles of -50°, 0°, and 50° respectively.

B. Real Data Results

In this section, we present reconstructions of real data using the new MBIR algorithm and compare it to reconstructions using traditional methods.

1) Data: A dedicated Lorentz TEM equipped with a spherical aberration corrector was used to image a NiFe sample patterned into interacting islands using vector field electron tomography [2], [48]. At each tilt angle, the electron phase is recovered from measurements using the transport-of-intensity phase retrieval algorithm presented in [4]. The data consists of electron phase images at tilt angles ranging from -50° to 50° at steps of 1° for tilt across both the u-axis and v-axis. The phase images at tilt angles of -50°, 0°, and 50° for tilt across the u-axis are shown in Fig. 7(a)–(c). Similarly, the phase images at the same tilt angles but for tilt across the v-axis are shown in Fig. 7(d)–(f).

2) Reconstruction: Fig. 8(a)–(f) shows the MBIR reconstruction of the 3D magnetization. There is no other conventional reconstruction shown since we could not find any other implementation of an algorithm that reconstructs 3D magnetization in the literature. We can see that the vertically aligned magnetic domains have magnetization oriented along the v-axis and the horizontally aligned magnetic domains have magnetization oriented along the u-axis.

Fig. 8(g)–(r) shows the reconstruction of the 3D magnetic vector potential using both MBIR and the conventional method presented in [2]. The conventional method results in prominent

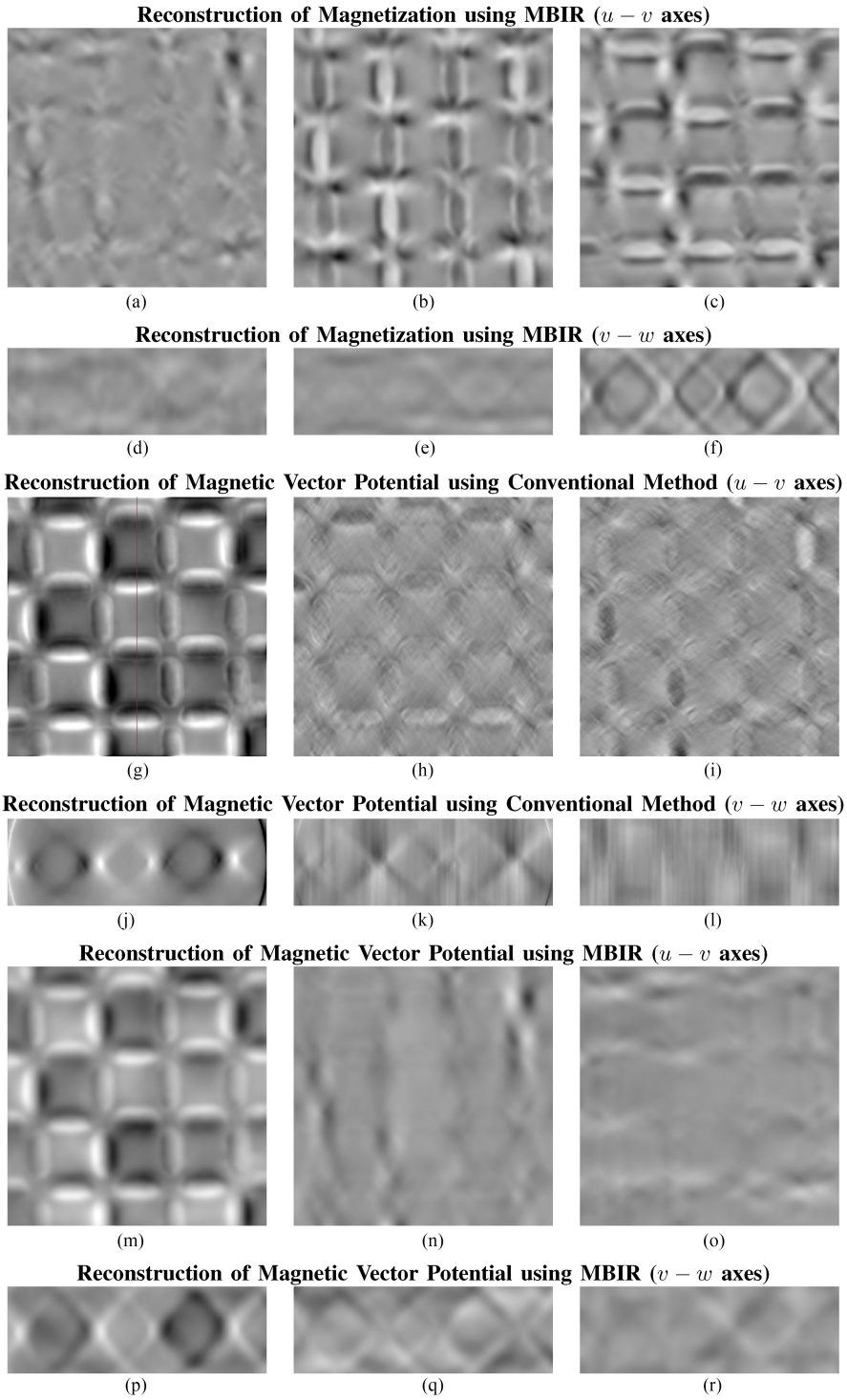

Fig. 8. Reconstructions of magnetization and magnetic vector potential of a Ni-Fe sample using the conventional method and MBIR. (a)–(c) and (d)–(f) show the reconstruction of magnetization using MBIR along the $u-v$ plane and $v-w$ plane respectively. (g)–(i) and (j)–(l) show the reconstruction of magnetic vector potential using the conventional method along the $u-v$ plane and $v-w$ plane respectively. (m)–(o) and (p)–(r) show the reconstruction of magnetic vector potential using MBIR along the $u-v$ plane and $v-w$ plane respectively. The 1st, 2nd, and 3rd columns show the vector field components oriented along the w-axis, v-axis, and u-axis respectively.

artifacts in the magnetic vector potential reconstruction of the v-axial component shown in Fig. 8(h) and (k) and the u-axial component shown in Fig. 8(i) and (l). Ideally, the u and v components of the magnetic vector potential must be zero. This is because the sample is engineered such that the w-axial component of magnetization is zero while the u-axis and v-axis components of magnetization do not vary along the w-axis. Hence, it follows that the u-axis and v-axis components of magnetic vector potential are zero from equations (4), (5), (7)–(9). From the root mean square error (RMSE) comparison in Table II, we can see

TABLE II
RMSE (NM^{-1}) BETWEEN THE MAGNETIC VECTOR POTENTIAL RECONSTRUCTION AND ZERO VALUED GROUND-TRUTH

	Conventional Method	MBIR
v-axial component	7.6×10^{-4}	7.0×10^{-4}
u-axial component	7.7×10^{-4}	6.4×10^{-4}

that the u and v axial reconstructions using MBIR have a lower RMSE than the conventional method.

3) Experimental Parameters: Each phase image has a resolution of 3.0 nm per pixel and a size of 384×384. All reconstructions of magnetization and magnetic vector potential have a voxel width of 3.0 nm.

The phase shift images in Fig. 7(a)–(f) are scaled from a minimum of -0.40 radians to a maximum of 0.43 radians. The images showing the magnetic vector potential in Fig. 8(g)–(r) are scaled from a minimum of -4×10^{-3} nm^{-1} to a maximum of 4×10^{-3} nm^{-1}. The images showing the magnetization in Fig. 8(a)–(f) are scaled from a minimum of -1.5×10^{-5} nm^{-2} to a maximum of 1.5×10^{-5} nm^{-2}. Note that the slices in Fig. 8(d)–(f), (j)–(l), and (p)–(r) go through the red colored line in Fig. 8(g).

V. CONCLUSION

In this paper, we presented an algorithm to reconstruct a sample's 3D magnetization from data acquired using transmission electron microscopy (TEM) experiments. This algorithm was formulated using the framework of MBIR. It uses a forward model for the imaging system and a prior model for enforcing sparsity during reconstruction. Our algorithm is also capable of reconstructing magnetic vector potential in addition to magnetization. Furthermore, our algorithm also significantly reduces the artifacts that are typically seen in reconstructions of magnetic vector potential using conventional methods.

APPENDIX A
DISCRETE IMPLEMENTATION OF GREEN'S FUNCTION CONVOLUTION

We will express the individual vector components of $A(r)$ in terms of the vector components of $M(r)$ by expanding the vector cross-product in the convolution relation shown in equation (3). Let $M(r) = \left(M^{(u)}(r), M^{(v)}(r), M^{(w)}(r)\right)$ represent the three orthogonal vector components of magnetization, $M(r)$, along each of the orthogonal (u, v, w) coordinate axes. Similarly, the Green's function in (3) is expressed in terms of its components as $h_C(r) = \left(h_C^{(u)}(r), h_C^{(v)}(r), h_C^{(w)}(r)\right)$ where

$$h_C^{(u)}(u,v,w) = \frac{u}{|u^2+v^2+w^2|^{3/2}}, \tag{41}$$

$$h_C^{(v)}(u,v,w) = \frac{v}{|u^2+v^2+w^2|^{3/2}}, \tag{42}$$

$$h_C^{(w)}(u,v,w) = \frac{w}{|u^2+v^2+w^2|^{3/2}}. \tag{43}$$

Then, the corresponding orthogonal components of the magnetic vector potential denoted by $A^{(u)}(r)$, $A^{(v)}(r)$, and $A^{(w)}(r)$ are given by

$$A^{(u)}(r) = \frac{\mu_0}{4\pi}\int_{\mathcal{R}^3}\Big[M^{(v)}(r')h_C^{(w)}(r-r') - M^{(w)}(r')h_C^{(v)}(r-r')\Big]\,dr', \tag{44}$$

$$A^{(v)}(r) = \frac{\mu_0}{4\pi}\int_{\mathcal{R}^3}\Big[M^{(w)}(r')h_C^{(u)}(r-r') - M^{(u)}(r')h_C^{(w)}(r-r')\Big]\,dr', \tag{45}$$

$$A^{(w)}(r) = \frac{\mu_0}{4\pi}\int_{\mathcal{R}^3}\Big[M^{(u)}(r')h_C^{(v)}(r-r') - M^{(v)}(r')h_C^{(u)}(r-r')\Big]\,dr'. \tag{46}$$

To derive a discrete approximation to equations (44)–(46), it is necessary to first formulate discrete approximations to the Green's functions in (41)–(43). This is done by substituting $(u,v,k) = (i\Delta, j\Delta, k\Delta)$ in (41)–(43) where Δ is the sampling width (voxel width). However, the sampled value at $(i=0, j=0, k=0)$ is undefined since $h_C^{(u)}(u,v,w) \to \infty, h_C^{(v)}(u,v,w) \to \infty$, and $h_C^{(w)}(u,v,w) \to \infty$ as $u \to 0, v \to 0$, and $w \to 0$. To prevent numerical instabilities due to the singularity at the origin, we will approximate the value at $(0,0,0)$ by integrating (41)–(43) over a voxel cube of width Δ centered at $(0,0,0)$. Thus, an approximation to the value at $(0,0,0)$ for $h_C^{(u)}(u,v,w)$ is

$$\int_{w=-\frac{\Delta}{2}}^{\frac{\Delta}{2}}\int_{v=-\frac{\Delta}{2}}^{\frac{\Delta}{2}}\int_{u=-\frac{\Delta}{2}}^{\frac{\Delta}{2}} h_C^{(u)}(u,v,w)\,du\,dv\,dw \tag{47}$$

$$= \int_{w=-\frac{\Delta}{2}}^{\frac{\Delta}{2}}\int_{v=-\frac{\Delta}{2}}^{\frac{\Delta}{2}}\left[\int_{u=-\frac{\Delta}{2}}^{0}\frac{u}{|u^2+v^2+w^2|^{3/2}}\right. \tag{48}$$

$$\left. + \int_{u=0}^{\frac{\Delta}{2}}\frac{u}{|u^2+v^2+w^2|^{3/2}}\right]du\,dv\,dw \tag{49}$$

$$= \int_{w=-\frac{\Delta}{2}}^{\frac{\Delta}{2}}\int_{v=-\frac{\Delta}{2}}^{\frac{\Delta}{2}}\left[\int_{u=-\frac{\Delta}{2}}^{0}\frac{u}{|u^2+v^2+w^2|^{3/2}}\right. \tag{50}$$

$$\left. - \int_{u=-\frac{\Delta}{2}}^{0}\frac{u}{|u^2+v^2+w^2|^{3/2}}\right]du\,dv\,dw \tag{51}$$

$$= 0. \tag{52}$$

The above approximation computes the Cauchy principal value of the integral in equation (47). It eliminates the possibility of numerical instabilities that will otherwise occur due to the unbounded nature of the Green's function at the origin.

The Green's function in (41)–(43) have infinite support along each of the (u,v,w) axes. If we abruptly cut-off the support of these functions using a rectangular window, it will result in ringing artifacts in the reconstruction of magnetization. To avoid such artifacts, we use a smooth window function such as a Hamming window to limit the support of (41)–(43). Thus, our

discrete approximations to the Green's functions are,

$$\tilde{h}_D^{(u)}[i,j,k] = W[i,j,k]\frac{i}{|i^2+j^2+k^2|^{3/2}\Delta^2}, \tag{53}$$

$$\tilde{h}_D^{(v)}[i,j,k] = W[i,j,k]\frac{j}{|i^2+j^2+k^2|^{3/2}\Delta^2}, \tag{54}$$

$$\tilde{h}_D^{(w)}[i,j,k] = W[i,j,k]\frac{k}{|i^2+j^2+k^2|^{3/2}\Delta^2}, \tag{55}$$

where $\tilde{h}_D^{(u)}[0,0,0] = \tilde{h}_D^{(v)}[0,0,0] = \tilde{h}_D^{(w)}[0,0,0] = 0$ and $W[i,j,k] = W_u[i]W_v[j]W_w[k]$ is a 3D window function where $W_u[i]$, $W_v[j]$, and $W_w[k]$ are 1D Hamming windows. Since discrete convolution is implemented using discrete summation rather than continuous domain integration, the differential terms du, dv, and dw in (3) are accounted for by the sample width, Δ. Thus, Δ is absorbed into the expressions $\tilde{h}_D^{(u)}[i,j,k]$, $\tilde{h}_D^{(v)}[i,j,k]$, and $\tilde{h}_D^{(w)}[i,j,k]$. Thus, the modified point spread functions that are used to compute the magnetic vector potential using discrete convolution are given by

$$h_D^{(u)}[i,j,k] = W[i,j,k]\frac{i\Delta}{|i^2+j^2+k^2|^{3/2}}, \tag{56}$$

$$h_D^{(v)}[i,j,k] = W[i,j,k]\frac{j\Delta}{|i^2+j^2+k^2|^{3/2}}, \tag{57}$$

$$h_D^{(w)}[i,j,k] = W[i,j,k]\frac{k\Delta}{|i^2+j^2+k^2|^{3/2}}. \tag{58}$$

Let $x^{(u)}$, $x^{(v)}$, and $x^{(w)}$ be vector arrays containing all voxel values of $M^{(u)}(r)$, $M^{(v)}(r)$, and $M^{(w)}(r)$ respectively. We can then express the vectors arrays $z^{(u)}, z^{(v)}$, and $z^{(w)}$ containing the voxel values of $A^{(u)}(r)$, $A^{(v)}(r)$, and $A^{(w)}(r)$ respectively as

$$z^{(u)} = H^{(w)}x^{(v)} - H^{(v)}x^{(w)}, \tag{59}$$

$$z^{(v)} = H^{(u)}x^{(w)} - H^{(w)}x^{(u)}, \tag{60}$$

$$z^{(w)} = H^{(v)}x^{(u)} - H^{(u)}x^{(v)}, \tag{61}$$

where $H^{(u)}$, $H^{(v)}$, and $H^{(w)}$ are matrices that implement 3D convolution with the point spread functions in (56), (57), and (58) respectively. Before performing convolution, we symmetrically zero-pad the 3D volume vectors $x^{(u)}$, $x^{(v)}$, and $x^{(w)}$ to twice its width along each spatial dimension. The width of the window function $W[i,j,k]$ along each dimension is equal to half the width of the zero-padded volumes. Zero padding is necessary to avoid artifacts caused by circular convolution in equations (59), (60), and (61).

Appendix B
Parameters of Tomographic Inversion Update

In this appendix, we will present closed-form expressions for the gradient ω and Hessian Ω in (32). The error sinogram vectors in (33) and (34) can be rewritten in terms of the matrices $P^{(u)}$ and $P^{(v)}$ as

$$e_i^{(u)} = y_i^{(u)} - P_i^{(u)}\left(-z^{(v)}\sin\left(\theta_i^{(u)}\right) + z^{(w)}\cos\left(\theta_i^{(u)}\right)\right),$$

$$e_j^{(v)} = y_j^{(v)} - P_j^{(v)}\left(-z^{(u)}\sin\left(\theta_j^{(v)}\right) + z^{(w)}\cos\left(\theta_j^{(v)}\right)\right).$$

If ω_i is the ith element of the 3×1 vector ω, we can show that

$$\omega_1 = \frac{1}{\sigma^2}\sum_{j=1}^{M_v} e_j^{(v)t} P_{j,*,k}^{(v)} \sin\left(\theta_j^{(v)}\right), \tag{62}$$

$$\omega_2 = \frac{1}{\sigma^2}\sum_{i=1}^{M_u} e_i^{(u)t} P_{i,*,k}^{(u)} \sin\left(\theta_i^{(u)}\right), \tag{63}$$

$$\omega_3 = -\frac{1}{\sigma^2}\sum_{j=1}^{M_v} e_j^{(v)t} P_{j,*,k}^{(v)} \cos\left(\theta_j^{(v)}\right) - \frac{1}{\sigma^2}\sum_{i=1}^{M_u} e_i^{(u)t} P_{i,*,k}^{(u)} \cos\left(\theta_i^{(u)}\right), \tag{64}$$

where M_u and M_v are the total number of tilt angles across the u-axis and v-axis respectively and $P_{i,*,k}^{(u)}$ and $P_{j,*,k}^{(v)}$ represent the elements of the kth column of the projection matrices $P_i^{(u)}$ and $P_j^{(v)}$ respectively (defined in (13) and (14)). Similarly, if $\Omega_{i,j}$ denotes the element at the ith row and jth column of the 3×3 Hessian matrix Ω, then

$$\Omega_{1,1} = \frac{1}{\sigma^2}\sum_{j=1}^{M_v}\left|\left|P_{j,*,k}^{(v)}\right|\right|^2 \sin^2\left(\theta_j^{(v)}\right), \tag{65}$$

$$\Omega_{1,3} = \Omega_{3,1} = -\frac{1}{\sigma^2}\sum_{j=1}^{M_v}\left|\left|P_{j,*,k}^{(v)}\right|\right|^2 \sin\left(\theta_j^{(v)}\right)\cos\left(\theta_j^{(v)}\right), \tag{66}$$

$$\Omega_{2,2} = \frac{1}{\sigma^2}\sum_{i=1}^{M_u}\left|\left|P_{i,*,k}^{(u)}\right|\right|^2 \sin^2\left(\theta_i^{(u)}\right), \tag{67}$$

$$\Omega_{2,3} = \Omega_{3,2} = -\frac{1}{\sigma^2}\sum_{i=1}^{M_u}\left|\left|P_{i,*,k}^{(u)}\right|\right|^2 \sin\left(\theta_i^{(u)}\right)\cos\left(\theta_i^{(u)}\right), \tag{68}$$

$$\Omega_{3,3} = \frac{1}{\sigma^2}\sum_{j=1}^{M_v}\left|\left|P_{j,*,k}^{(v)}\right|\right|^2 \cos^2\left(\theta_j^{(v)}\right) + \frac{1}{\sigma^2}\sum_{i=1}^{M_u}\left|\left|P_{i,*,k}^{(u)}\right|\right|^2 \cos^2\left(\theta_i^{(u)}\right), \tag{69}$$

$$\Omega_{1,2} = \Omega_{2,1} = 0. \tag{70}$$

Appendix C
Efficient Implementation of Deconvolution Step

The gradient vector $g = \left[g^{(u)t}, g^{(v)t}, g^{(w)t}\right]$ in (38) can be reformulated in terms of $H^{(u)}$, $H^{(v)}$, and $H^{(w)}$ as

$$g^{(u)} = -\mu \left[H^{(w)t} f^{(v)} - H^{(v)t} f^{(w)} \right] + B^{(u)} x^{(u)}, \quad (71)$$

$$g^{(v)} = -\mu \left[H^{(u)t} f^{(w)} - H^{(w)t} f^{(u)} \right] + B^{(v)} x^{(v)}, \quad (72)$$

$$g^{(w)} = -\mu \left[H^{(v)t} f^{(u)} - H^{(u)t} f^{(v)} \right] + B^{(w)} x^{(w)}, \quad (73)$$

where

$$f^{(u)} = \left(H^{(w)} x^{(v)} - H^{(v)} x^{(w)} - z^{(u)} + t^{(u)} \right), \quad (74)$$

$$f^{(v)} = \left(H^{(u)} x^{(w)} - H^{(w)} x^{(u)} - z^{(v)} + t^{(v)} \right), \quad (75)$$

$$f^{(w)} = \left(H^{(v)} x^{(u)} - H^{(u)} x^{(v)} - z^{(w)} + t^{(w)} \right). \quad (76)$$

Thus, the gradient is computed efficiently since matrix multiplication with $H^{(u)}$, $H^{(v)}$, and $H^{(w)}$ is equivalent to linear space invariant convolution with the point spread functions in (7)–(9) respectively. And matrix multiplication with $H^{(u)t}$, $H^{(v)t}$, and $H^{(w)t}$ is equivalent to linear space invariant convolution with the space reversed version of the point spread functions in (7)–(9) respectively [42]. All convolution operations are implemented using FFT based Fourier transforms.

Similarly, the Hessian can be expressed in block-matrix representation as

$$Q = \begin{bmatrix} Q^{(uu)} & Q^{(uv)} & Q^{(uw)} \\ Q^{(vu)} & Q^{(vv)} & Q^{(vw)} \\ Q^{(wu)} & Q^{(wv)} & Q^{(ww)} \end{bmatrix}, \quad (77)$$

where

$$Q^{(uu)} = H^{(w)t} H^{(w)} + H^{(v)t} H^{(v)} + B^{(u)}, \quad (78)$$

$$Q^{(vv)} = H^{(w)t} H^{(w)} + H^{(u)t} H^{(u)} + B^{(v)}, \quad (79)$$

$$Q^{(ww)} = H^{(v)t} H^{(v)} + H^{(u)t} H^{(u)} + B^{(w)}, \quad (80)$$

$$Q^{(uv)} = -H^{(u)t} H^{(v)},\ Q^{(vu)} = -H^{(v)t} H^{(u)}, \quad (81)$$

$$Q^{(uw)} = -H^{(u)t} H^{(w)},\ Q^{(wu)} = -H^{(w)t} H^{(u)}, \quad (82)$$

$$Q^{(vw)} = -H^{(v)t} H^{(w)},\ Q^{(wv)} = -H^{(w)t} H^{(v)}. \quad (83)$$

The stepsize α is then computed as

$$\alpha = \frac{\sum_{d \in \{u,v,w\}} g^{(d)t} g^{(d)}}{\sum_{d_1 \in \{u,v,w\}} \sum_{d_2 \in \{u,v,w\}} g^{(d_1)t} Q^{(d_1 d_2)} g^{(d_2)}}. \quad (84)$$

Similar to the computation of gradient, the computation of α is implemented using filtering operations.

REFERENCES

[1] P. Tartaj, M. del Puerto Morales, S. Veintemillas-Verdaguer, T. Gonzlez-Carreo, and C. J. Serna, "The preparation of magnetic nanoparticles for applications in biomedicine," *J. Phys. D: Appl. Phys.*, vol. 36, no. 13, 2003, Art. no. R182.

[2] C. Phatak, M. Beleggia, and M. D. Graef, "Vector field electron tomography of magnetic materials: Theoretical development," *Ultramicroscopy*, vol. 108, no. 6, pp. 503–513, 2008.

[3] S. Lade, D. Paganin, and M. Morgan, "Electron tomography of electromagnetic fields, potentials and sources," *Opt. Commun.*, vol. 253, no. 46, pp. 392–400, 2005.

[4] E. Humphrey, C. Phatak, A. Petford-Long, and M. D. Graef, "Separation of electrostatic and magnetic phase shifts using a modified transport-of-intensity equation," *Ultramicroscopy*, vol. 139, pp. 5–12, 2014.

[5] V. Stolojan, R. Dunin-Borkowski, M. Weyland, and P. Midgley, "Three-dimensional magnetic fields of nanoscale elements determined by electron-holographic tomography," *Inst. Phys., Conf. Ser.*, vol. 168, pp. 243–246, 1999/2001.

[6] E. Völkl, L. F. Allard, and D. C. Joy, *Introduction to Electron Holography*. New York, NY, USA: Springer, 1999.

[7] Y. Aharonov and D. Bohm, "Significance of electromagnetic potentials in the quantum theory," *Phys. Rev.*, vol. 115, no. 3, pp. 485–491, 1959.

[8] C. Phatak and D. Gursoy, "Iterative reconstruction of magnetic induction using lorentz transmission electron tomography," *Ultramicroscopy*, vol. 150, pp. 54–64, 2015.

[9] R. P. Yu, M. J. Morgan, and D. M. Paganin, "Lorentz-electron vector tomography using two and three orthogonal tilt series," *Phys. Rev. A*, vol. 83, Feb. 2011, Art. no. 023813.

[10] L. Desbat and A. Wernsdorfer, "Direct algebraic reconstruction and optimal sampling in vector field tomography," *IEEE Trans. Signal Process.*, vol. 43, no. 8, pp. 1798–1808, Aug. 1995.

[11] B. K. Horn and B. G. Schunck, "Determining optical flow," *Artif. Intell.*, vol. 17, no. 1, pp. 185–203, 1981.

[12] N. Papenberg, A. Bruhn, T. Brox, S. Didas, and J. Weickert, "Highly accurate optic flow computation with theoretically justified warping," *Int. J. Comput. Vision*, vol. 67, no. 2, pp. 141–158, 2006.

[13] T. Schuster, "An efficient mollifier method for three-dimensional vector tomography: Convergence analysis and implementation," *Inverse Problems*, vol. 17, no. 4, pp. 739–766, 2001.

[14] N. F. Osman and J. L. Prince, "3D vector tomography on bounded domains," *Inverse Probl.*, vol. 14, no. 1, pp. 185–196, 1998.

[15] G. Sparr, K. Strahlen, K. Lindstrom, and H. W. Persson, "Doppler tomography for vector fields," *Inverse Probl.*, vol. 11, no. 5, pp. 1051–1061, 1995.

[16] K. M. Holt, "Angular regularization of vector-valued signals," in *Proc. IEEE Int. Conf. Acoust., Speech, Signal Process.*, May 2011, pp. 1105–1108.

[17] D. Keren and A. Gotlib, "Denoising color images using regularization and "correlation terms," *J. Vis. Comun. Image Represent.*, vol. 9, no. 4, pp. 352–365, Dec. 1998.

[18] M. Arigovindan, M. Suhling, C. Jansen, P. Hunziker, and M. Unser, "Full motion and flow field recovery from echo doppler data," *IEEE Trans. Med. Imag.*, vol. 26, no. 1, pp. 31–45, Jan. 2007.

[19] P. D. Tafti and M. Unser, "On regularized reconstruction of vector fields," *IEEE Trans. Image Process.*, vol. 20, no. 11, pp. 3163–3178, Nov. 2011.

[20] A. Kovcs *et al.*, "Mapping the magnetization fine structure of a lattice of bloch-type skyrmions in an FeGe thin film," *Appl. Phys. Lett.*, vol. 111, no. 19, 2017, Art. no. 192410.

[21] J. Caron, J. Ungermann, R. E. Dunin-Borkowski, and M. Riese, "Towards electron holography of 3D magnetization distributions in nanoscale materials using a model-based iterative reconstruction technique," in *Proc. 18th Int. Microscopy Congr.*, 2014.

[22] J. Caron, P. Diehle, A. Kovcs, J. Ungermann, and R. E. Dunin-Borkowski, "Model-based reconstruction of magnetisation distributions in nanostructures from electron-optical phase images," in *Proc. Annu. Conf. Yocomat*, 2017.

[23] R. E. Dunin-Borkowski *et al.*, "Limitations and challenges in off-axis electron holography of electromagnetic fields in nanoscale materials," in *Proc. Eur. Microscopy Congr.*, 2016, pp. 677–678.

[24] K. A. Mohan *et al.*, "TIMBIR: A method for time-space reconstruction from interlaced views," *IEEE Trans. Comput. Imag.*, vol. 1, no. 2, pp. 96–111, Jun. 2015.

[25] K. A. Mohan *et al.*, "4D model-based iterative reconstruction from interlaced views," in *Proc. IEEE Int. Conf. Acoust., Speech, Signal Process.*, Apr. 2015, pp. 783–787.

[26] K. A. Mohan, S. Venkatakrishnan, L. Drummy, J. Simmons, D. Parkinson, and C. Bouman, "Model-based iterative reconstruction for synchrotron X-ray tomography," in *Proc. IEEE Int. Conf. Acoust., Speech, Signal Process.*, May 2014, pp. 6909–6913.

[27] Z. Ruoqiao, J. B. Thibault, C. A. Bouman, K. D. Sauer, and H. Jiang, "Model-based iterative reconstruction for dual-energy X-ray CT using a joint quadratic likelihood model," *IEEE Trans. Med. Imag.*, vol. 33, no. 1, pp. 117–134, Jan. 2014.

[28] C. Bouman and K. Sauer, "A unified approach to statistical tomography using coordinate descent optimization," *IEEE Trans. Image Process.*, vol. 5, no. 3, pp. 480–492, Mar. 1996.

[29] K. A. Mohan, X. Xiao, and C. A. Bouman, "Direct model-based tomographic reconstruction of the complex refractive index," in *Proc. IEEE Int. Conf. Image Process.*, Sep. 2016, pp. 1754–1758.
[30] X. Wang, K. A. Mohan, S. J. Kisner, C. Bouman, and S. Midkiff, "Fast voxel line update for time-space image reconstruction," in *Proc. IEEE Int. Conf. Acoust., Speech, Signal Process.*, Mar. 2016, pp. 1209–1213.
[31] K. A. Mohan, "Design of 4D X-ray tomography experiments for reconstruction using regularized iterative algorithms," *Proc. SPIE*, vol. 10391, 2017, Art. no. 103910U.
[32] S. Venkatakrishnan, L. Drummy, M. Jackson, M. De Graef, J. Simmons, and C. Bouman, "Model-based iterative reconstruction for bright field electron tomography," *IEEE Trans. Comput. Imag.*, vol. 1, no. 1, pp. 1–15, Mar. 2015.
[33] S. Sreehari *et al.*, "Plug-and-play priors for bright field electron tomography and sparse interpolation," *IEEE Trans. Comput. Imag.*, vol. 2, no. 4, pp. 408–423, Dec. 2016.
[34] S. V. Venkatakrishnan, L. F. Drummy, M. A. Jackson, M. De Graef, J. Simmons, and C. A. Bouman, "A model based iterative reconstruction algorithm for high angle annular dark field-scanning transmission electron microscope (HAADF-STEM) tomography," *IEEE Trans. Image Process.*, vol. 22, no. 11, pp. 4532–4544, Nov. 2013.
[35] K. Prabhat, K. A. Mohan, C. Phatak, C. Bouman, and M. D. Graef, "3D reconstruction of the magnetic vector potential using model based iterative reconstruction," *Ultramicroscopy*, vol. 182, pp. 131–144, 2017.
[36] K. A. Mohan, K. C. Prabhat, C. Phatak, M. D. Graef, and C. A. Bouman, "Iterative reconstruction of the magnetization and charge density using vector field electron tomography," *Microscopy Microanal.*, vol. 22, no. S3, pp. 1686–1687, 2016.
[37] K. A. Mohan, "Modular forward models and algorithms for regularized reconstruction of time-space scalar and vector fields," Ph.D. dissertation, Purdue Univ., West Lafayette, IN, USA, 2017.
[38] E. K. Chong and S. H. Zak, *An Introduction to Optimization*, vol. 76. New York, NY, USA: Wiley, 2013.
[39] M. Beleggia and Y. Zhu, "Electron-optical phase shift of magnetic nanoparticles I. Basic concepts," *Philosoph. Mag.*, vol. 83, no. 8, pp. 1045–1057, 2003.
[40] M. Beleggia, Y. Zhu, S. Tandon, and M. D. Graef, "Electron-optical phase shift of magnetic nanoparticles II. Polyhedral particles," *Philosoph. Mag.*, vol. 83, no. 9, pp. 1143–1161, 2003.
[41] M. D. Graef, *Introduction to Conventional Transmission Electron Microscopy*. Cambridge, U.K.: Cambridge Univ. Press, 2003.
[42] C. A. Bouman, *Model Based Image Processing*, 2013. [Online]. Available: https://engineering.purdue.edu/bouman/publications/pdf/MBIP-book.pdf
[43] X. Wang, A. Sabne, P. Sakdhnagool, S. J. Kisner, C. A. Bouman, and S. P. Midkiff, "Massively parallel 3D image reconstruction," in *Proc. Int. Conf. High Perform. Comput., Netw., Storage Anal.*, 2017, Art. no. 3.
[44] S. Boyd, N. Parikh, E. Chu, B. Peleato, and J. Eckstein, "Distributed optimization and statistical learning via the alternating direction method of multipliers," *Found. Trends Mach. Learn.*, vol. 3, no. 1, pp. 1–122, 2011.
[45] B. S. He, H. Yang, and S. L. Wang, "Alternating direction method with self-adaptive penalty parameters for monotone variational inequalities," *J. Optim. Theory Appl.*, vol. 106, no. 2, pp. 337–356, 2000.
[46] S. L. Wang and L. Z. Liao, "Decomposition method with a variable parameter for a class of monotone variational inequality problems," *J. Optim. Theory Appl.*, vol. 109, no. 2, pp. 415–429, 2001.
[47] M. Kamasak, C. Bouman, E. Morris, and K. Sauer, "Direct reconstruction of kinetic parameter images from dynamic PET data," *IEEE Trans. Med. Imag.*, vol. 24, no. 5, pp. 636–650, May 2005.
[48] C. Phatak, A. Petford-Long, O. Heinonen, M. Tanase, and M. De Graef, "Nanoscale structure of the magnetic induction at monopole defects in artificial spin-ice lattices," *Phys. Rev. B*, vol. 83, no. 17, May 2011, Art. no. 174431.

K. Aditya Mohan (SM'08–M'18) received the B.Tech. degree in electronics and communication engineering from the National Institute of Technology Karnataka, Surathkal, India, in 2010, and the M.S. and Ph.D. degrees in electrical and computer engineering from Purdue University, West Lafayette, IN, USA, in 2014 and 2017, respectively. He is currently a Signal and Image Processing Postdoctoral Researcher with the Computational Engineering Division, Lawrence Livermore National Laboratory, Livermore, CA, USA. His research interests include computational imaging, inverse problems, statistical signal processing, and machine learning.

Prabhat KC received the B.A. degree in mathematics from Mercyhurst University, Erie, PA, USA, in 2012, and the Ph.D. degree in materials science and engineering from Carnegie Mellon University, Pittsburgh, PA, in 2017. His research interests include tomographic reconstruction using limited data, inverse problems, statistical image processing, and algorithms on convex optimization.

Charudatta Phatak received the Ph.D. degree from Carnegie Mellon University, Pittsburgh, PA, USA, in 2009. He is a Staff Scientist with the Materials Science Division, Argonne National Laboratory, Lemont, IL, USA. He has authored or coauthored more than 50 publications in the area of magnetic imaging and transmission electron microscopy. His research interests include understanding domain behavior in magnetic heterostructures, 3-D tomographic reconstruction of scalar and vector fields, and the integrated imaging approach for electron and X-ray microscopy.

Marc De Graef received the B.S. and M.S. degrees in physics from the University of Antwerp, Antwerp, Belgium, in 1983, and the Ph.D. degree in physics with a thesis on copper-based shape memory alloys from the Catholic University of Leuven, Leuven, Belgium, in 1989. He then spent three and a half years as a Postdoctoral Researcher with the Materials Department, University of California at Santa Barbara, before joining Carnegie Mellon University, Pittsburgh, PA, USA, in 1993, where he is currently a Professor and co-Director of the J. Earle and Mary Roberts Materials Characterization Laboratory. His research interests include material characterization by means of electron microscopy and X-ray tomography techniques. He is a fellow of the Microscopy Society of America. He was a recipient of the 2012 Educator Award from the Minerals, Metals, and Materials Society.

Charles A. Bouman (F'01) received the B.S.E.E. degree from the University of Pennsylvania, Philadelphia, PA, USA, in 1981, the M.S. degree from the University of California at Berkeley, CA, USA, in 1982, and the Ph.D. degree in electrical engineering from Princeton University, Princeton, NJ, USA, in 1989.

From 1982 to 1985, he was a full staff member with MIT Lincoln Laboratory. In 1989, he joined the faculty of Purdue University, West Lafayette, IN, USA, where he is currently the Showalter Professor of electrical and computer engineering and biomedical engineering. His research resulted in the first commercial model-based iterative reconstruction system for medical X-ray computed tomography. He is a co-inventor on more than 50 issued patents that have been licensed and used in millions of consumer imaging products. His research interests include statistical signal and image processing with applications ranging from medical to scientific and consumer imaging. He is a member of the National Academy of Inventors, a fellow of the American Institute for Medical and Biological Engineering, a fellow of the Society for Imaging Science and Technology (IS&T), and a fellow of the SPIE Professional Society. He is the recipient of the 2014 Electronic Imaging Scientist of the Year Award and the IS&T's Raymond C. Bowman Award. He has been a Purdue University Faculty Scholar and received the College of Engineering Engagement/Service Award and Team Award. He was also the Founding co-Director of Purdue's Magnetic Resonance Imaging Facility from 2007 to 2016 and the Chair of Purdue's Integrated Imaging Cluster from 2012 to 2016. He was the Editor-in-Chief for the IEEE TRANSACTIONS ON IMAGE PROCESSING, a Distinguished Lecturer for the IEEE Signal Processing Society, and a Vice President of Technical Activities for the IEEE Signal Processing Society, during which time he lead the creation of the IEEE TRANSACTIONS ON COMPUTATIONAL IMAGING. He is an Associate Editor for the IEEE TRANSACTIONS ON IMAGE PROCESSING, the IEEE TRANSACTIONS ON PATTERN ANALYSIS AND MACHINE INTELLIGENCE, and the *SIAM Journal on Mathematical Imaging*. He has also been a Vice President of Publications and a member of the Board of Directors for the IS&T Society. He is the Founder and co-Chair of the SPIE/IS&T Conference on Computational Imaging.